

Impact of nanostructure configuration on the photovoltaic performance of quantum dot arrays

Aude Berbezier*¹ and Urs Aeberhard¹

IEK5-Photovoltaik, Forschungszentrum Jülich, 52425 Jülich, Germany

In this work, an effective quantum model based on the non-equilibrium Green's function formalism is used to investigate a selectively contacted high density quantum dot array in a wide band gap host matrix for operation as a quantum dot-enhanced single junction solar cell. By establishing a direct relation between nanostructure configuration and optoelectronic properties, the investigation reveals the influence of inter-dot and dot-contact coupling strength on the radiative rates and consequently on the ultimate performance of photovoltaic devices with finite quantum dot arrays as the active medium. The dominant effects originate in the dependence of the Joint Density of States on the inter-dot coupling in terms of band width and effective band gap.

In a large variety of concepts for next generation solar cells, nanostructures like quantum wells, wires or dots provide the specific physical properties required to reach beyond current efficiency limitations¹⁻³. Among these nanostructures, quantum dots (QD) are of special interest due to their largely tunable optoelectronic characteristics, and QD structures thus represent promising candidates for the implementation of novel high efficiency solar cell concepts^{4,5}. However, to enable exploitation of the design degrees of freedom provided, the complex relation between structural configuration parameters and device characteristics requires thorough investigation. In conventional macroscopic modeling approaches, this connection is provided only indirectly via macroscopic material parameters such as absorption coefficient, mobility and lifetime of charge carriers⁶. For a direct, consistent and comprehensive assessment of configuration related photovoltaic performance, both interband dynamics and transport of charge carriers need to be described in a unified microscopic picture, like the one provided by the non-equilibrium Green's function (NEGF) formalism⁷. Since a fully microscopic treatment of extended systems of coupled QD comes with a huge computational cost, application of multi-scale approaches is indicated, such as the mesoscopic QD orbital tight-binding model introduced in Ref. 8.

Here, this model is used in a simplified version, with restriction to a single orbital per band, phenomenological nearest-neighbor hopping parameters and flat band conditions. These simplifications assure maximum transparency in the analysis of the photovoltaic mechanisms in the QD arrays considered. In this way, clear relations can be established between configuration dependent properties on one side, such as the finite system size, the coupling between QD and the presence and nature of contacts, and the photovoltaic performance on the other side. With the above simplifications, the phenomenological Hamiltonian of the device shown schematically in Fig. 1 reads for a given carrier species $b \in \{c, v\}$:

$$\hat{\mathcal{H}}_0^b = - \sum_{i=1}^{N_{QD}-1} t_{b,ii+1} \left[\hat{d}_{b,i+1}^\dagger \hat{d}_{b,i} + h.c. \right] + \sum_{i=1}^{N_{QD}} \varepsilon_{b,i} \hat{n}_{b,i} \quad (1)$$

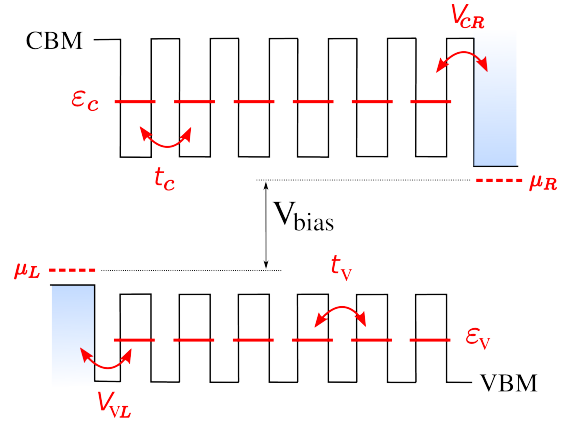


FIG. 1. (color online) Schematic band diagram and phenomenological parameters characterizing the selectively contacted QD array. The carrier selectivity of the contacts is required for photocurrent rectification at flat band conditions in the absence of a doping induced junction. While the contacts are assumed to be equilibrated with charge carrier populations characterized by chemical potentials μ_L and μ_R , respectively, the carrier population inside the absorber emerges from the quantum-statistical formalism.

where N_{QD} is the number of dots, t_b is the inter-dot coupling, $\hat{n}_b \equiv \hat{d}_b^\dagger \hat{d}_b$ is the carrier density operator and ε_b is the QD energy level. This Hamiltonian is used in the equations for the steady state charge carrier NEGF, which read for a given band and energy E :

$$\mathbf{G}^R(E) = \left[\{\mathbf{G}_0^R(E)\}^{-1} - \Sigma^{RI}(E) - \Sigma^{RC}(E) \right]^{-1}, \quad (2)$$

$$\mathbf{G}^{\lessgtr}(E) = \mathbf{G}^R(E) \left[\Sigma^{\lessgtr I}(E) + \Sigma^{\lessgtr C}(E) \right] \mathbf{G}^A(E), \quad (3)$$

$$\mathbf{G}_0^R(E) = [(E + i\eta)\mathbb{1} - \mathbf{H}_0]^{-1}, \quad \mathbf{G}^A(E) = [\mathbf{G}^R(E)]^\dagger,$$

where $\mathbf{G} \equiv [G_{ij}]$ with $G_{ij}(E) = \int d\tau e^{iE\tau/\hbar} G_{ij}(\tau)$, $\tau = t' - t$ and $G_{ij}(t, t') = -\frac{i}{\hbar} \langle \hat{T}_C \{ \hat{d}_i(t) \hat{d}_j^\dagger(t') \} \rangle$ the ensemble average ordered on the Keldysh contour⁹. The self-energy (SE) terms Σ^C encode the hybridization of QD and contact states, enabling the description of charge car-

rier extraction and injection at the electrodes:

$$\Sigma_{ij}^{RB}(E) = -\frac{i}{2}\delta_{ij}\Gamma(E), \quad (4)$$

$$\Sigma_{ij}^{\leq B}(E) = i\left[f(E - \mu_B) - \frac{1}{2} \pm \frac{1}{2}\right]\delta_{ij}\Gamma(E), \quad (5)$$

where $B \in \{L, R\}$, f is the Fermi-Dirac distribution function, μ_B is the chemical potential of the contact considered, and the broadening function Γ_B is related to the coupling parameter V_B and the density of states (DOS) ρ_B of the electrode through $\Gamma_B(E) = V_B^2\rho_B(E)$. In the following, a bulk-like DOS is assumed for the contact states. In order to achieve the carrier selectivity required for charge separation and current rectification in the absence of a built-in potential, the contact couplings are set to zero at the minority carrier boundaries, which are chosen at the left electrode for electrons and at the right electrode for holes (see also Fig. 1).

At this level, the formalism provides the electronic structure of the non-interacting system under arbitrary non-equilibrium conditions, e.g., via the local density of charge carrier states $\rho_i(E) = -\frac{1}{\pi}\Im G_{ii}^R(E)$. Figure 2 displays the LDOS for an array of 20 coupled QD together with the total DOS obtained from summing the individual QD contributions. In contrast to standard simulations of QD-based solar cells, where extended QD superlattices are modeled using periodic boundary conditions^{10,11}, discrete states can still be distinguished in the total DOS. On the other hand, the main effect of the presence of a contact is the broadening of the LDOS, especially in the vicinity of the electrode, where the band width is strongly increased from the limiting value of $\sim 4t_b$ of the infinite single orbital tight-binding (TB) chain, which is nearly recovered in arrays with as few as 20 QD. The energy integration of the total DOS yields N_{QD} , in agreement with the associated sum rule.

The SE terms Σ^I include the interactions relevant for the photovoltaic device operation, i.e., coupling to photons, phonons and to other charge carriers (not considered in this work). For the coupling of charge carriers to electromagnetic fields, stimulated and spontaneous processes need to be distinguished. Since photovoltaic devices are operated above room temperature, thermal broadening is considered via the physical line-shape provided by quasi-elastic coupling to phonons.

Photogeneration and stimulated emission induced by incident radiation is described via the SE for the interaction with a classical field with vector potential \mathbf{A} ,¹²

$$\begin{aligned} \Sigma_{ij,\eta}^{e\gamma-st,\leq}(E, \hbar\omega) &= \mathcal{M}_i^{e\gamma,\eta}\mathcal{M}_j^{e\gamma,\eta} \left\{ G_{ij}^{\leq}(E - \hbar\omega) \right. \\ &\left. + G_{ij}^{\leq}(E + \hbar\omega) \right\} A_\eta(\mathbf{R}_i, \hbar\omega) A_\eta(\mathbf{R}_j, \hbar\omega), \end{aligned} \quad (6)$$

with $\hbar\omega$ the photon energy, $\eta \in \{x, y, z\}$ the polarization component and the coupling matrix elements $\mathcal{M}_i^{e\gamma,\eta} \equiv -\left(\frac{e}{m_0}\right)\mathbf{p}_{cv}^\eta(\mathbf{R}_i)$, where \mathbf{p}_{cv} is the interband momentum matrix element and \mathbf{R}_i the QD position. The attenuation of the EM field relates to the absorption cross section

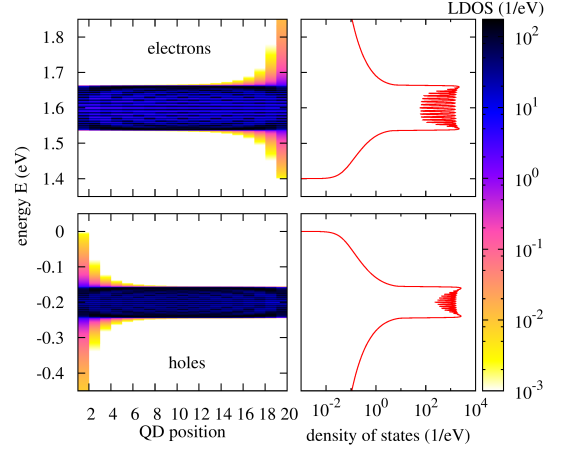


FIG. 2. (color online) Local and total density of electron and hole states for a selectively contacted 20 QD array with $V_c = V_v = 1$ eV, $t_c = 0.03$ eV and $t_v = 0.02$ eV. At the closed contacts, the band width approaches the infinite single orbital TB chain value of $4t_b$. At the open contacts on the contrary, the hybridization with contact states induces a pronounced widening of the bands.

(AC) \mathcal{A} of the QD array via the absorption coefficient $\alpha(\hbar\omega) = \rho_{QD}\mathcal{A}(\hbar\omega)$, where ρ_{QD} is the QD density. The AC itself is computed based on the electronic structure from the net spectral absorption rate and the incident photon flux via $\mathcal{A}_\eta(\hbar\omega) \equiv R_{abs,net}^\eta(\hbar\omega)/\Phi_{0\eta}^\gamma(\hbar\omega)$, with

$$\begin{aligned} \mathcal{R}_{abs,net}^\eta(\hbar\omega) &= \int \frac{dE}{2\pi\hbar} \sum_{i,j} \left[G_{ij}^>(E)\Sigma_{ji}^{e\gamma-st,<}(E, \hbar\omega) \right. \\ &\left. - G_{ij}^<(E)\Sigma_{ji}^{e\gamma-st,>}(E, \hbar\omega) \right], \end{aligned} \quad (7)$$

and $\Phi_{0\eta}^\gamma(\hbar\omega) = 2n_r c_0 \varepsilon_0 \hbar^{-1}\omega |A_\eta(\mathbf{R}_0, \hbar\omega)|^2$, where a background refractive index n_r is assumed. This yields the following expression for the AC in terms of the photon SE Π

$$\mathcal{A}_\eta(\hbar\omega) = \frac{c_0}{2n_r\omega} \sum_{i,j} \Re\{i\hat{\Pi}_{ji,\eta\eta}(\hbar\omega)\}. \quad (8)$$

Expression (8) considers the net absorptance, i.e., including stimulated emission, by the definition of $\hat{\Pi} \equiv \Pi^> - \Pi^<$ from the photon SE components $\Pi_{ij,\eta\eta'}^{\leq}(E) = -i\hbar\mu_0\mathcal{M}_i^{e\gamma,\eta}\mathcal{M}_j^{e\gamma,\eta'}\mathcal{P}_{ij}^{\leq}(E)$, where the electron-hole polarization function elements are $\mathcal{P}_{nm}^{\leq}(E) = \int \frac{dE'}{2\pi\hbar} G_{nm}^{\leq}(E')G_{mn}^{\geq}(E' - E)$, and which is hence related to the spectral function $\hbar\hat{\mathcal{P}}/2\pi$ of occupied electron-hole pairs¹³. At global quasi-equilibrium conditions and far away from degeneracy, band filling effects can be neglected, and the spectral function is proportional to the Joint Density of States (JDOS) of the system, which in turn can be written in terms of the spectral functions of the individual charge carriers as follows:

$$\mathcal{J}_{cv}(E) = \pi^{-2} \int dE' \text{tr} \left\{ \Im \mathbf{G}_c^R(E') \Im \mathbf{G}_v^R(E' - E) \right\}. \quad (9)$$

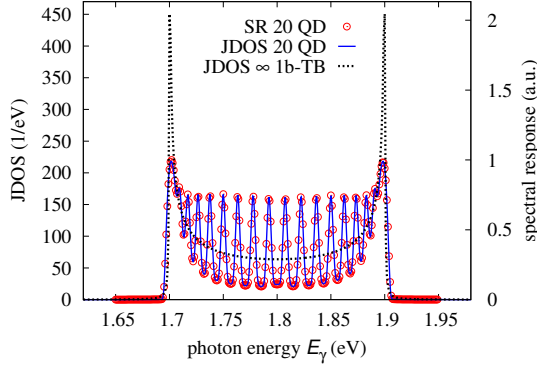


FIG. 3. (color online) Joint Density of States (JDOS) and Spectral Response (SR) of the 20 QD cell as obtained from the NEGF, in comparison with the JDOS of the infinite 1D TB model.

Figure 3 shows the JDOS for a system of 20 coupled and selectively contacted QD (solid line), together with the JDOS for the infinite 1D TB chain (dotted line). While the band width of the finite system is almost identical to that of the infinite chain, the spectral distribution of the JDOS differs considerably, from clearly distinguishable contributions of individual dots to a smooth continuum.

The spectral response (SR) of the system can be obtained directly from the evaluation for a given monochromatic illumination of the general NEGF expression $I_i^e = \frac{e}{\hbar} \int \frac{dE}{\pi} 2\text{Re} \{H_{0,ii+1} G_{i+1i}^<(E)\}$ for the electron current in the conduction band between QDs at positions \mathbf{R}_i and \mathbf{R}_{i+1} ¹⁴. A similar expression exists for the hole current I^h in the valence band in terms of the hole NEGF $G^>$. The total current $I^{tot} = I^e + I^h$ can be compared to the photocurrent as given by the absorptance and the photon flux via the spectral current relation $I_A(\hbar\omega) = e \sum_{\eta} \Phi_{\eta}^{\gamma}(\hbar\omega) \mathcal{A}_{\eta}(\hbar\omega) \equiv e \mathcal{R}_{abs,net}(\hbar\omega)$. The collection efficiency for the photogenerated charge carriers is then given by the ratio $\eta_{coll} = I^{tot}/I_A$. In the situation displayed in Fig. 3 (empty dots), the total photocurrent is directly proportional to the JDOS, which is explained by the use of constant momentum matrix elements, the absence of bleaching effects and unit extraction efficiency.

At the radiative limit, the dark current-voltage characteristics of the selectively contacted QD array solar cell is determined by the current due to radiative recombination of charge carriers injected at the contacts. For the description of the associated spontaneous emission process, consideration of the photon Green's function of the entire system is required to include all the optical modes with finite coupling. Under the assumption of an optically homogeneous medium, use of the free field photon propagator results in the SE¹⁵

$$\Sigma_{ij}^{e\gamma-sp,\leq}(E) \approx \frac{\mu_0 n_r}{\pi c_0} \bar{\mathcal{M}}_i^{e\gamma} \bar{\mathcal{M}}_j^{e\gamma} \int_0^{\infty} \frac{dE'}{2\pi\hbar} E' G_{ij}^{\leq}(E \pm E'), \quad (10)$$

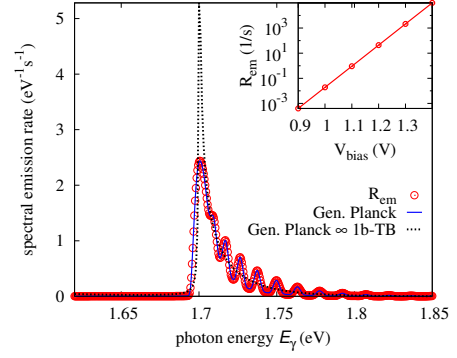


FIG. 4. (color online) Spectral emission rate for the 20 QD cell as derived from the NEGF formalism (empty dots) as well as from the Generalized Planck law using the NEGF absorption (solid line) or the infinite 1D TB model (dotted line). The inset shows the integrated emission rate as a function of V_{bias} .

where $\bar{\mathcal{M}}$ are the polarization-averaged coupling elements. In terms of the photon SE, the polarization-averaged spectral emission rate of the QD array acquires the form

$$\bar{\mathcal{R}}_{em}(\hbar\omega) = \frac{n_r \omega}{2\pi^2 \hbar c_0} \sum_{i,j} \Re \{i\bar{\Pi}_{ji}^<(\hbar\omega)\}, \quad (11)$$

which is obtained by using $\Sigma^{e\gamma-sp}$ in the expression for the emission rate in analogy to Eq. (7). For valid assumption of a *global* quasi-equilibrium, the *Kubo-Martin-Schwinger* relation between the components of the polarization function^{16,17}, $\mathcal{P}^<(\hbar\omega) = \mathcal{P}^>(\hbar\omega) e^{-\beta(\hbar\omega - \mu_{cv})}$, with $\beta = (k_B T)^{-1}$ and $\mu_{cv} = \mu_c - \mu_v$ the quasi-Fermi level splitting (QFLS), can be used in Expr. (8) and (11) to derivation the *Generalized Planck* law¹⁸ via the connection¹⁹

$$\bar{\mathcal{R}}_{em}(\hbar\omega) = \bar{\mathcal{A}}(\hbar\omega) \frac{(\hbar\omega)^2 n_r^2}{\pi^2 \hbar^3 c_0^2} \left\{ e^{\beta(\hbar\omega - \mu_{cv})} - 1 \right\}^{-1}. \quad (12)$$

To obtain the QFLS, the individual QFL μ_c and μ_v of electrons and holes in conduction and valence bands need to be determined. They can be defined via the carrier density and the spectral function $\hat{G} \equiv -2\Im G^R$ under the assumption of local quasi-equilibrium conditions, in which the fluctuation-dissipation theorem provides the relations $G_c^{\leq}(E) = i\hat{G}_c(E) [f(E - \mu_c) - 1/2 \pm 1/2]$. An energy independent value of the QFL is extracted from the density determined via energy integration of G^{\leq} . Figure 4 shows the comparison of the electroluminescence spectra as obtained from the NEGF via the above formalism for the 20 QD system at $V_{bias} = 1.1$ V (empty dots) with the Generalized Planck emission for AC determined either via NEGF for the same finite system (solid line) or for the infinite TB chain (dotted line). The effective emission edge of the 20 QDs cell is close to the one of the infinite 1D TB model, as expected from the convergence of the spectral width of the JDOS seen in Fig. 3.

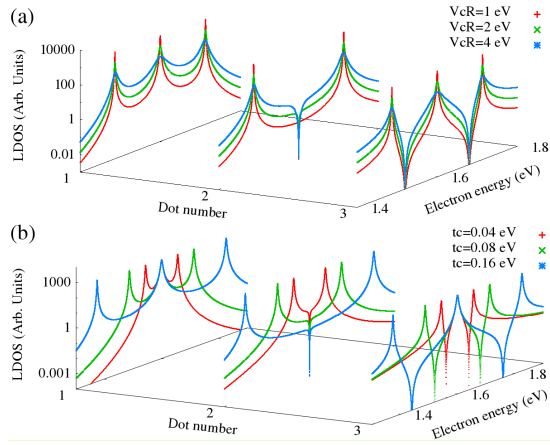


FIG. 5. (color online) Local density of electron states of a right-contacted 3 QD system for varying values of (a) the contact coupling V_{cR} and (b) the inter-dot coupling t_c .

The linear increase of the QFLS with V_{bias} results in an exponential growth of the emission rate (inset of Fig. 4).

On the basis of this general analysis, the specific impact of the dot-contact and inter-dot coupling on the density of states, spectral response and radiative recombination characteristics can now be discussed. Figure 5(a) displays the LDOS of electrons in a 3 QD chain contacted from the right. The hybridization of the discrete QDs levels with the continuum of bulk electrode states introduces Fano-type asymmetric features close to the contact, which gradually disappear with increasing distance from the electrode. The main effect of the presence of this contact is the broadening of the LDOS, especially in the vicinity of the electrode, where the band width can be strongly increased as shown previously in Fig. 2. Since

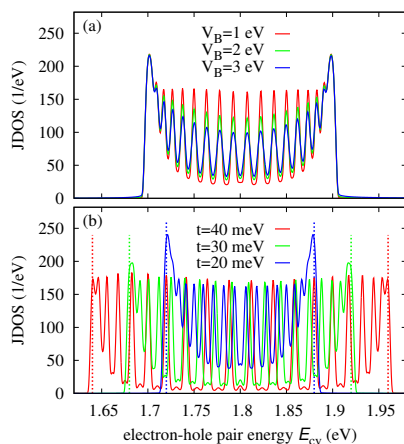


FIG. 6. (color online) The JDOS for the 20 QD cell is presented in (a) for various values of contact coupling $V_{cR} = V_{vL}$ at $t_{c/v} = 0.03/0.02$ eV and in (b) for different inter-dot coupling parameters $t = t_c = t_v$ at $V_{cR} = V_{vL} = 1$ eV (dashed lines indicate band width of 1D TB chain).

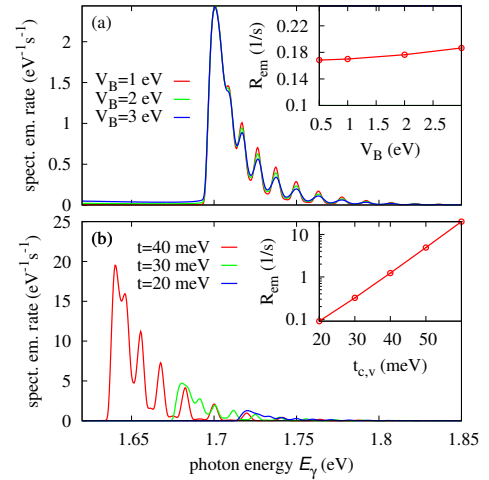


FIG. 7. (color online) Spectral emission rate for the 20 QDs cell as a function of the photon energy, in (a) for different contact couplings and in (b) for different inter-dot couplings. The inset displays the corresponding variation of the integrated emission rate.

the electrode self-energy has no real part, the magnitude of V_{cR} only affects this broadening, but does not induce any shift in the resonance peaks. As can be inferred from Fig. 5(b), the inter-dot coupling acts on the LDOS mainly via the direct relation to the miniband width. In Fig. 6(a), the spread in energy of the individual dot contributions is determined by the contact induced broadening. The width of the JDOS is determined by the inter-dot coupling in analogy to the DOS of the individual bands and converges with increasing number of dots to that of the single orbital TB chain (dashed lines). Figure 7 (a) and (b) show the impact of contact and inter-dot coupling strength on the levels of radiative dark current generation. Since the effective gap is not directly affected by the contact coupling, there is only a slight increase of the dark current with stronger contact hybridization due to the induced smearing of the emission edge, as displayed in Fig. 7(a). On the other hand, Fig. 7(b) reveals the exponential increase of the recombination with inter-dot coupling strength due to the linear decrease of effective band gap $\varepsilon_{cv}^{eff} = \varepsilon_{cv}^0 - 2(t_c + t_v)$, i.e., of the energy of the dominant contribution to the overall emission process.

In conclusion, we used a customized NEGF simulation framework to provide a direct relation between the local nanostructure configuration and the global photovoltaic device performance of a finite and selectively contacted QD array. The dominant effects result from the dependence of the JDOS on inter-dot coupling and system size in terms of spectral shape, band-width and effective gap. The analysis can be extended to more complex descriptions of the local electronic structure and to any kind of disorder affecting the charge carrier transport and hence the extraction efficiency.

- ¹M. A. Green, "Potential for low dimensional structures in photovoltaics," *Mater. Sci. Eng. B*, **74**, 118 (2000), ISSN 0921-5107.
- ²A. Martí, *Next generation photovoltaics : high efficiency through full spectrum utilization*, Series in optics and optoelectronics (IOP, Bristol, 2004) pp. XI, 332 S.
- ³L. Tsakalacos, "Nanostructures for photovoltaics," *Mater. Sci. Eng., R*, **62**, 175 (2008), ISSN 0927-796X.
- ⁴A. Nozik, "Quantum dot solar cells," *Physica E*, **14**, 115 (2002).
- ⁵A. Martí, N. López, E. Antolín, E. Cánovas, C. Stanley, C. Farmer, L. Cuadra, and A. Luque, "Novel semiconductor solar cell structures: The quantum dot intermediate band solar cell," *Thin Solid Films*, **511 - 512**, 638 (2006).
- ⁶V. Aroutiounian, S. Petrosyan, and A. Khachatryan, "Studies of the photocurrent in quantum dot solar cells by the application of a new theoretical model," *Sol. Energy Mater. Sol. Cells*, **89**, 165 (2005), ISSN 09270248.
- ⁷U. Aeberhard, "Theory and simulation of quantum photovoltaic devices based on the non-equilibrium Greens function formalism," *J. Comput. Electron.*, **10**, 394 (2011), ISSN 1569-8025.
- ⁸U. Aeberhard, "Effective microscopic theory of quantum dot superlattice solar cells," *Opt. Quantum. Electron.*, **44**, 133 (2012), ISSN 0306-8919.
- ⁹L. Keldysh, "Diagram technique for nonequilibrium processes," *Sov. Phys. JETP*, **20**, 1018 (1965).
- ¹⁰C.-W. Jiang and M. A. Green, "Silicon quantum dot superlattices: Modeling of energy bands, densities of states, and mobilities for silicon tandem solar cell applications," *J. Appl. Phys.*, **99**, 114902 (2006).
- ¹¹S. Tomić, T. S. Jones, and N. M. Harrison, "Absorption characteristics of a quantum dot array induced intermediate band: Implications for solar cell design," *Appl. Phys. Lett.*, **93**, 263105 (2008).
- ¹²U. Aeberhard, "Quantum-kinetic theory of steady-state photocurrent generation in thin films: Coherent versus incoherent coupling," *Phys. Rev. B*, **89**, 115303 (2014).
- ¹³U. Aeberhard, "Quantum-kinetic theory of photocurrent generation via direct and phonon-mediated optical transitions," *Phys. Rev. B*, **84**, 035454 (2011).
- ¹⁴R. K. Lake and R. R. Pandey, "Non-equilibrium green functions in electronic device modeling," in *Handbook of Semiconductor Nanostructures*, edited by A. A. Balandin and K. L. Wang (American Scientific Publishers, 2006).
- ¹⁵U. Aeberhard, "Simulation of nanostructure-based and ultra-thin film solar cell devices beyond the classical picture," *J. Photon. Energy*, **4**, 042099 (2014).
- ¹⁶M. F. Pereira and K. Henneberger, "Microscopic theory for the influence of coulomb correlations in the light-emission properties of semiconductor quantum wells," *Phys. Rev. B*, **58**, 2064 (1998).
- ¹⁷F. Richter, M. Florian, and K. Henneberger, "Generalized radiation law for excited media in a nonequilibrium steady state," *Phys. Rev. B*, **78**, 205114 (2008).
- ¹⁸P. Würfel, "The chemical potential of radiation," *J. Phys. C: Solid State Phys.*, **15**, 3967 (1982).
- ¹⁹Strictly, this relation between absorption at zero bias an emission under finite QFLS is only valid if neither JDOS nor the optical matrix elements $\mathcal{M}^{e\gamma}$ are modified at finite bias voltage, e.g., due to a change in orbital overlap or local band bending.